13. 朝川直行、小林誠一、後藤純一、平山令明「AutoGPA モデルによる受容体ポケットの特徴抽出」第 **37** 回構造活性相関シンポジウム (東京) 北里大学薬学部 2009 年 11 月 12 日
14. 小林誠一、朝川直行、後藤純一、平山令明「AutoGPA:グリッドとファーマコフォアモデルの連携による 3D-QSAR モデルの自動構築」第 **37** 回構造活性相関シンポジウム (東京) 北里大学薬学部 2009 年 11 月 13 日
15. 平山令明「PLB 法を用いた低分子結合部位の差別化」第 10 回 日本バイオインフォマティクス学会創薬インフォマティクス研究会「活性ポケットをインフォマティクスで理解する」(東京) 産総研 臨海副都心センター2009 年 12 月 2 日

厚生科学研究費補助金　（医療機器開発推進研究事業ナノメディシン研究）

分担研究報告書

ナノ分子イメージングを活用した次世代創薬アプローチ

分担研究項目　創薬標的タンパクの構造解析 - 1

分担研究者　武田　壮一　　国立循環器病センター研究所心臓生理部　室長

盛　英三　　東海大学医学部基礎医学系　教授

研究要旨：循環器疾患、脳神経疾患等の制圧のためにナノ分子イメージングを活用して新しい治療法の開発を推進することを目的とする。本分担研究では、分子の構造決定に基づく創薬を目指した研究を行う。本年度の標的タンパクとしてADAMTS13のエキソサイトドメインの構造解析を行った。2.6Å分解能の精密構造を得ることに成功し、基質VWFの認識部位を同定することができた。ADAMTS13の機能不全による血栓性血小板減少性紫斑病(TTP)の発症メカニズムの理解と新しい治療法開発がより進むことが期待される。

A．研究目的

ADAMTS13は血漿von Willebrand因子(VWF)を切断するメタロプロテアーゼである。遺伝的もしくは自己抗体の出現などにより後天的にADAMTS13活性が欠損すると、血中に超高分子量VWFマルチマーが蓄積し、これが微小血管で血小板血栓形成を引き起こし、重篤な疾患である血栓性血小板減少性紫斑病(TTP)を生じる。本研究ではADAMTS13の機能不全によるTTP発症のメカニズムの解明と新しい治療法の開発を目的にADAMTS13のVWF認識ドメインを含む領域ADAMTS13-DTCS(287-685アミノ酸残基)の結晶構造の決定を行った。

B．研究方法

ADAMTS13-DTCSを糖鎖修飾酵素変異株CHO Lec 3.2.8.1に分泌発現させ、各種クロマトグラフィーにより精製した。単離したADAMTS-DTCSを用いてSitting-drop法により結晶化スクリーニングを行った。得られた単結晶についてSPring-8のアンジュレーター ビームラインBL41XUを用いて回折データ収集を行った。$OsCl_3$を含む重原子置換体結晶を用い、OsのL3吸収端近傍の4波長回折強度データセットを用いて実験的に2.9Å分解能での位相決定を行い、最終的には2種類の重原子を含まない結晶を用いて2.6Åおよび2.8Åでの精密化を行い、構造決定を行った。結晶構造を基に様々な変異ADAMTS-MDTCS分子を作成し、VWF切断活性を測定した。

C．研究結果

全てのADAMTSファミリータンパク質は分子N末端側からメタロプロテアーゼ(M)、ディスインテグリン様(D)、thrombospondin type-1 (T)、システインリッチ(C)およびスペーサー(S)の各ドメインを共通して持ち、このMDTCSドメイン部がADAMTSファミリータンパク質の機能に重要であることが分かっている。今回我々はこれらの機能ドメインの内ADAMTS13のMドメインを除くDTCS部について構造決定を行った。既に欧米グループが他のADAMTSについてMD部の構造決定を報告していたので、これらと合わせMDTCSドメイン部全体のモデルを世界で初めて提案することが出来た。その他、(1) Dドメイン全体とCドメインのN末側領域(C_A)は、アミノ酸配列の相同性は17%しかないにもかかわらず、構造的に近縁のADAMファミリータンパク質のCドメインと相同な折り畳み構造をとること、(2) T1ドメインの立体構造が先に構造解析されたthrombospondin-1とよく一致すること、(3) Cドメインの C末側領域(C_B)はC_AとSドメインとの連結ドメインであること、(4) Sドメインは10本のβストランドからなる2枚のアンチパラレルなβシートからなる構造ドメインであること、(5) C_AドメインとSドメインは複数の残基を介して相互作用していること、などが明らかになった。さらに、得られた立体構造を元に変異体を作成し、それらの

VWF切断活性を測定することでADAMTS13の分子表面にVWF認識部位をマッピングすることに成功した。

D．考察

新たに解明した立体構造とそれに基づく変異体解析からADAMTS13の分子表面に存在するいくつかの可変ループ部が協同して伸展したVWFを認識するメカニズムが明らかになった。

E．結論

今回の結晶構造解析により全てのADAMTS分子に共通した基本構造が明らかになった。変形性関節炎(OA)に深く関与するアグリカナーゼ(ADAMTS4およびADAMTS5)はOA治療薬のターゲットと考えられている。我々の立体構造はこれらアグリカナーゼのexosite inhibitorの設計などにも役立つと考えられる。

G．研究発表

（研究業績「欧文」）

【原著】

1. Nakayama D, Ben Ammar, Takeda S. "Crystallization and preliminary X-ray crystallographic analysis of the blood coagulation factor V-activating proteinase (RVV-V) from Russell's viper venom" ***Acta Cryst***, F65, 1306-1308, (2009)
2. Akiyama, M, Takeda S, Kokame, K, Takagi, J, Miyata, T. "Crystal structures of the non-catalytic domains of ADAMTS13 reveal multiple discontinuous exosites for von Willebrand factor" ***Proc Natl Acad Sci USA.***, 106, 19274-19279 (2009)
3. Akiyama, M, Takeda S, Kokame, K, Takagi, J, Miyata, T. "Production, crystallization and preliminary crystallographic analysis of the exosite-containing fragment of human von Willebrand factor-cleaving proteinase, ADAMTS13" ***Acta Cryst***, F65: 739-742, (2009)
4. K.Yamada, R.Kuroda, H.Toyakawa, H.Ikeura-Sekiguchi, M.Yasumoto, M.Koike, F.Sakai, K.Mori, H.Mori, N.Fukuyama, E.Sato: A trial for fine and low-dose imaging of biological specimens using quasi-monochromatic laser-Compton X-rays: Nuclear Instruments and Methods in Physics Research.2009; A 608: S7–S10
5. T.Nishikawa, N.Iwakiri, Y.Kaneko, A.Taguchi, K.Fukushima, H.Mori, N.Morone, J.Kadokawa: Nitric Oxide Release in Human Aortic Endothelial Cells Mediated by Delivery of Amphiphilic Polysiloxane Nanoparticles to Caveolae: Biomacromolecules. 2009; 10: 2074–2085

（研究業績「和文」）

【総説】

1. 武田壮一「ADAMファミリー蛋白質の立体構造と作用機構」特集・膜蛋白質の切断とその制御 蛋白質核酸酵素 54(13), 1754-1759 (2009)
2. 武田壮一「蛇毒メタロプロテアーゼの立体構造とラッセルクサリヘビ毒素によるX因子活性化機構」血栓止血学会誌 20(3), 307-314 (2009)

【学会発表】

1. Takeda S, Akiyama M, Kokame K, Takagi J, Miyata T: "Crystal structures of the non-catalytic domains of ADAMTS13", Gordon Research Conference: Matrix Metalloproteinases, Les Diablerets, Switzerland, 2009.9.2-3 (poster)
2. "H.Mori: A creative care approach to the elderly with cognitive impairment in a group home in japan: 25th International Conference of Alzheimer's Disease International, 10-13 March 2010, Thessaloniki, Macedonia - Greece"
3. H.Mori, T.Fujii, N.Fukuyama, Y.Ikeya, Y.Shinozaki, K.Fukushima, K.Umetani, T.Tanabe: Fingertip microangiography using synchrotron radiation toward prediction of diabetic angiopathy: European Congress of Radiology, March 4–8, 2010, in Vienna, Austria.
4. H.Mori, T.Fujii, N.Fukuyama, Y.Ikeya, Y.Shinozaki, K.Umetani, T.Tanabe: Development of Fingertip Microangiography using Synchrotron Radiation to. Determine Fixed Combination in the Treatment of Metabolic Syndrome.: The 2 International Conference on Fixed Combination in the Treatment of Hypertension, Dyslipidemia and Diabetes Mellitues 10-12 December 2009. Valencia, Spain.

5. T.Yada, H.Shimokawa, O.Hiramatsu, M.Satoh, N.Kashihara, Y.Shinozaki, H.Mori, A.Takaki, M.Goto, H.Nakamoto, Y.Ogasawara, F.Kajiya: Cardioprotective Effect of Hydrogen Peroxide and Erythropoietin During Acute Coronary Occlusion in Canine Coronary Native Collateral Microvessels in vivo: American Heart Association (Orland, Florida)
6. 中山大輔、Ben Ammar Youssef、武田壮一「ラッセルクサリヘビ毒由来血液凝固第 V 因子活性化プロテアーゼの X 線結晶構造解析」日本結晶学会年会、関西学院大学、2009.6(口頭発表)
7. 中山大輔、Ben Ammar Youssef、武田壮一「ラッセルクサリヘビ毒由来血液凝固第 V 因子活性化プロテアーゼの構造解析」第 82 回日本生化学会大会、神戸国際会議場、2009.10(ポスターおよび口頭発表)
8. 秋山正志、武田壮一、小亀浩市、高木淳一、宮田敏行「ADAMTS13 非触媒ドメインの結晶構造解析と von Willebrand 因子に対する複数の非連続エキソサイトの同定」第 82 回日本生化学会大会、神戸国際会議場、2009.10(ポスター)
9. 武田壮一「蛇毒プロテアーゼの結晶構造から見えてきた ADAM/ADAMTS ファミリープロテアーゼの作用機構」、SPC シンポジウム、第 32 回日本血栓止血学会学術集会、北九州国際会議場、2009.6.4(口頭発表)
10. 秋山正志、武田壮一、小亀浩市、高木淳一、宮田敏行「X 線解析による ADAMTS13 の部分立体構造の決定とエキソサイトの同定」、SPC シンポジウム、第 32 回日本血栓止血学会学術集会、北九州国際会議場、2009.6.4(口頭発表)
11. 武田壮一、秋山正志、小亀浩市、高木淳一、宮田敏行「ADAMTS13 の部分結晶構造と von Willebrand 因子認識・切断機構」、第 9 回日本蛋白質科学会年会、熊本全日空ホテルニュースカイ、2009.5.21(ポスター発表)
12. T.Yada, H.Shimokawa, O.Hiramatsu, Y.Shinozaki, H.Mori, M.Goto, Y.Ogasawara, F.Kajiya: Role of H_2O_2 as an Endogenous EDHF during Coronary Occlusion and Injection of Erythropoietin in Canine Coronary Native Collateral Microvessels: 第 73 回日本循環器学会総会・学術集会. 2009
13. Y.Ikeya, N.Fukuyama, T.Fujii, S.Takeshita, K.Nishigami, Y.Tsutumi, H.Mori: In-hospital Microangiography for Vascular Regeneration Therapy: 第 73 回日本循環器学会総会・学術集会. 2009

H. 知的財産権の出願・登録状況

特に無し

厚生科学研究費補助金　（医療機器開発推進研究事業）
ナノ分子イメージングを活用した次世代創薬アプローチ
分担研究報告書
次期治療標的タンパクの構造解析－２

分担研究者　増田　道隆　　国立循環器病センター研究所循環器形態部室長

研究要旨：循環器疾患、脳神経疾患等の制圧のためにナノテクノロジーを駆使して、治療法の開発を推進することを目的とする。本分担研究では、分子の構造決定に基づく創薬を目指した研究を行う。本年度も引き続き、脂質結合・変形活性をもつ共通のドメイン構造を有する細胞内情報伝達分子タンパク群（BARドメインスーパーファミリータンパク質）の構造および機能相関を解析する。これを、基盤情報として次世代創薬に貢献する。

A. 研究目的

脂質膜結合・変形タンパク質

生体膜のリモデリングは、膜輸送や飲・食作用、細胞やオルガネラの形状形成などの基盤をなす重要な細胞活性である。この活性は細胞骨格と膜変形分子の共同作用として実現されている。アクチン細胞骨格の制御に中心的な役割を果たしているRhoファミリー低分子GTP結合タンパク質のエフェクター分子の中に、アクチン細胞骨格制御活性とともに脂質膜結合・変形活性をもつ新規のタンパク質ファミリー（BARドメインスーパーファミリー）に属する分子I-BARファミリーがあることが明らかにされた。I-BARの代表といえるIRSp53や、Ferキナーゼなどの F-BARドメインの構造研究は、生体膜のダイナミックスの制御をターゲットとした次世代創薬の可能性を開くものである。これらの分子機能の詳細を明らかにするため、タンパク結晶構造解析に取り組み、構造を基にしたデザイン変異体の機能解析から脂質膜変形能の分子的基盤を解明する。今年度も引き続きFerキナーゼを主たるターゲットとして研究を進めた。

FerとFes はSH3ドメインを持たない代わりに、脂質膜結合・変形ドメイン（F-BARドメイン）を持つ特異な非受容体型のチロシンキナーゼである。Ferは細胞接着制御に関わり、特に内皮細胞では接着分子のリン酸化を介して透過性を制御している。我々は、内皮細胞の細胞間接着分子PECAM-1のキナーゼとしてFerを同定し報告している。また、Fer/Fesは一部の癌の増悪化にも関係することが知られている。Fer/Fesは、ほとんどが細胞質に存在することから、F-BARドメインは活性が負に制御されていることが考えられる。逆にキナーゼ活性はF-BARドメインにより負に制御されているとの報告がある。脂質膜結合活性や、ドメイン間制御の詳細を明らかにするため、FerのF-BARドメインおよび全長のタンパク結晶構造解析に取り組んだ。

B. 研究方法

Ferの全長およびF-BARドメインの結晶を作製し、Ｘ線回折法により構造を決定する。また、構造に基づくデザイン変異体を多数作成し、機能解析により

膜変形能の構造的基盤を明らかにする。

C. 研究結果

心臓生理部・ベン-アマー室長および武田室長との共同研究により、Ferキナーゼの N-末端側に位置する F-BARドメインの結晶構造解析に成功した（図）。F-BARドメインの基本骨格は Tocaファミリーの F-BARドメインと類似していたが、これらのF-BARの特徴である二量体間の端-端結合サイトは保存されていなかった。さらに、BARスーパーファミリーで広く保存されている、膜結合表面のリジンやアルギニンの一部を欠いていることがわかった。構造を基に多数の変異体をデザインし、それらの脂質膜結合・変形活性を解析した。その結果、Ferの低い脂質膜結合・変形活性は、SH2-キナーゼドメインによる負の制御のためではなく、それ自体の活性が低いことによることが明らかになった。F-BARのC端側にあるCoiled-coilドメインは膜結合を強める働きがあること、F-BARドメインのどの部域の正電荷が膜結合・変形活性に重要であるかを明らかにする知見を得た。これらの結果については論文作成中である

全長については、効率的なタンパク発現に成功したが、現時点では分解能が７Åと低い結晶しか得られておらず、構造解析に至っていない。

C. 考察

Ferキナーゼの結晶構造の解明により、Ferファミリーキナーゼの特異的性質を明らかにするとともに、脂質結合・変形活性がどのように遮蔽されているか、逆に、どのようにしたら発揮されるのかについて示唆を得ることができた。局在とキナーゼ活性の制御メカニズムの詳細を明らかにすることにより、内皮細胞の透過性制御や機械刺激受容を調節する薬剤の開発につながる可能性がある。またこれらの研究は、新たな細胞生物学の研究領域の創成に資する。

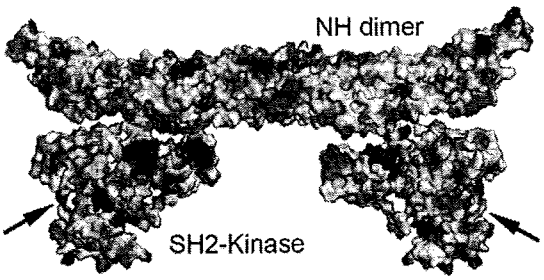

図　Ferキナーゼの構造モデル

今回明らかにしたのはバナナ形をしているN-末端の二量体であり、凹型の脂質膜結合表面を上向きに置いた。SH2-キナーゼはFesの構造(Filippakopoulos et al. Cell, 2008)よりモデル化した。N-末端とSH2の間には約60アミノ酸のリンカーがあり、これら3つの部分構造の関係は不明。この図では、正の表面電荷を持つSH2のリガンド結合サイトが、負電荷を示すN-末端の凸型表面と相互作用し、キナーゼ活性部位(矢印)が外側を向くように置いた。赤は負、青は正の表面電荷を示す。

E. 結論

I-BARやF-BARの構造決定を行ない、生体膜のダイナミックスの制御をターゲットとした次世代創薬や新研究領域創成の手がかりをつかんだ。

F. 研究発表

（研究業績「欧文」）

【総説】

M. Masuda and N. Mochizuki: Structural characteristics of BAR domain superfamily to sculpt the membrane. Semin Cell Dev Biol, in press. doi:10.1016/j.semcdb.2010.01.010

H. 知的財産権の出願・登録

特になし

厚生科学研究費補助金　（医療機器開発推進研究事業：ナノメディシン研究）
分担研究報告書

ナノ分子機能イメージングを活用した次世代創薬アプローチ

分担研究者　国立循環器病センター研究所循環器形態部長　望月直樹

研究要旨　Src Homology2 -containing tyrosine phosphatase (SHP2)は脱リン酸化酵素にも関わらず、細胞を増殖させ、変異は先天性心疾患Noonan症候群の原因になっている。本分担研究ではSHP2の阻害薬のinsilicoスクリーニングによって候補化合物を同定するとともに、SHP2の酵素活性を測定するアッセイ系を開発した。

A. 研究目的

チロシン脱リン酸化酵素SHP2は、脱リン酸化酵素であるにも関わらず、低分子量Ras蛋白質の活性化によるErkの活性化を起こし、細胞の増殖促進に働く。従って、遺伝子変異　(PTP11NがSHP2の遺伝子名である)によりSHP2のアミノ酸変異がおきてSHP2が恒常的活性化型変異を起こした場合には、Noonan症候群、Leopard症候群といった先天性心疾患をともなる先天異常を起こしてしまう。　しかし、SHP2が如何にしてRas活性化（ひいては増殖作用）を有しているのか不明であったため治療法の開発の標的さえ見つからなかった。SHP2が病態に関与する疾患として胃癌も考えられている、ヘリコバクターピロリのCagＡ蛋白質に結合することでSHP2が活性化して、胃細胞の過剰増殖から医癌の発症に至る系や、若年性骨髄単球性白血病でもSHP2の異常が報告されている。

本研究ではSHP2酵素の基質の同定から、SHP2の阻害薬の候補化合物の探索ならびに、阻害効果の判定のためのアッセイ系の確立を目指した。

B. 研究方法

SHP2野生体ならびに変異体の発現plasmidの構築：SHP2はアミノ末端にSH2ドメインをタンデムに２個つながっている。Ｃ末端側1/2にチロシン脱リン酸化酵素活性があり、通常Ｎ末端とＣ末端が結合しているがSH2がリン酸化チロシンに結合することによって、解放されてS脱リン酸化酵素の活性部位が基質を認識することが可能となる。これが正常なシグナル伝達系でのSHP2の活性化機構であるが、PTP11Nの遺伝子変異によって生じりD61G, E76D, T42Aのアミノ酸変異によってSHP2が恒常的活性化型となる。本研究ではこれらの恒常的活性化型を細胞で発現するplasmidを構築した。またこれらの精製蛋白質を得るためにタグ付き蛋白質を発現させるようなプラスミドも構築した。また、ゼブラフィッシュにヒト型SHP2変異体を発現させるために、pCS2ベクターに変異SHP2をコードするcDNAを挿入した。

ゼブラフィッシュ：野生型ゼブラフィッシュはストレインＡＢを用いた。通常飼育で、夜ー昼サイクルを厳密に管理し、採卵を行った。一細胞期の卵にSHP2 D61G mRNAをインジェクションして数日間の観察をおこなった。心臓の形態、ならびに両眼間の距離ならびに両眼の大きさを指標にD61G変異体の発現によって、Noonan症候群の症状を呈するモデルを作成することができるか否かを検討した。心臓の形態変化は実体顕微鏡下で、イメージングソフトFluoviewを用いて画像を構築した後に計測を行って心臓、眼症状の異常を定量的に解析するように努めた。

SHP2の基質の同定：これまでにFocal adhesion kinaseがSHP2の基質となりうることが報告されていたがわれわれはERKの活性化を抑制する系の抑制系にSHP2が作用すると考えて、その基質の同定を試みた。

C. 研究結果

まず基質分子Ｘを同定した。：Ｘは、リン酸化部位を複数有しておりこのなかで近接するTyrのリン酸化ペプチドを用いて脱リン酸化活性を測定したところSH2をもつ分子が結合するTyrがSHP2によって効率よく脱リン酸化されることを突き止めた。さらに、この基質のリン酸化ペプチドを用いて、恒常的活性化型SHP2 (D61G, D61Yなど) を用いて脱リン酸化活性を測定したところ、顕著な脱リン酸化を認めた。一方、脱リン酸化不活性型ＳＨＰ２ (C/S)変異体では全く酵素反応が生じないことも確認した。

SHP2の構造解析からの予測によるSHP2阻害化合物候補分子の探索：SHP2の脱リン酸化酵素ドメインはすでに報告されており(3B70)、これをもとにしてSigma-Aldrichの化合物ライブラリーの6,500化合物のドッキング計算を行った。SHP2の構造のなかでmalate ionが結合する部位が存在し、二つの立体配座によって、候補を絞り込んだところ６０、３１の候補化合物にSHP2結合能があるのではないかと予想できる結果となった。

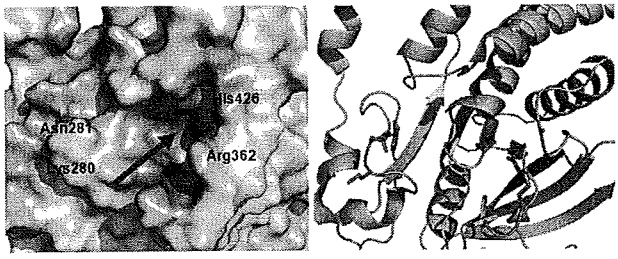

SHP2異常の疾患モデルとしてのゼブラフィッシュの有用性：D61G変異mRNAのinjectionにより心嚢の

拡大と、眼の縮小と、両眼の乖離が顕著となっており、Noonan症候群の症状を一致する所見をゼブラフィッシュでも呈することがわかった。またD61Y変異体のインジェクションでは、胚胎の形成の異常も認めら、Rasのシグナル活性化を示唆する所見もえられた。

野生型　　SHP2 D61G

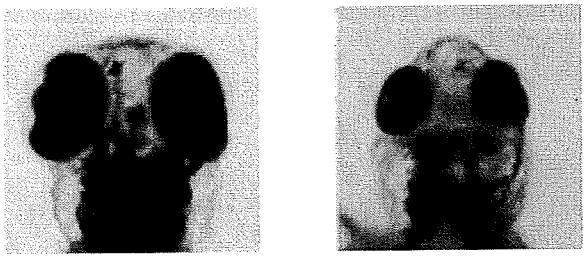

D. 考察

SHP2は癌・先天性心疾患・白血病の原因遺伝子となっていることからも創薬の対象となると考えた。先天性疾患であっても、症状を軽減することが可能であろう。また胃癌の発症にもSHP2シグナルの過剰反応がpirori菌によっておこることからも胃癌に対する治療薬の候補となりうる。さらにsomatic mutationがおきた場合には急性白血病の原因にもなるので、SHP2の阻害薬としての可能性は少なくとも３つの疾病で考えられる。

血このためにSHP2にまず結合活性があると予想できるものをスクリーニングの対象とした。化合物ライブラリーのなかで９０化合物をSHP2結合活性があると予想してSHP2阻害薬の候補化合物として選択することができた。われわれは本研究でSHP2の酵素活性を測定するアッセイ系を確立しており、９０の候補化合物について同アッセイで阻害効果の有無を検証可能である。

もし、阻害効果が認められればさらに、化合物の側鎖の改変によるより高効率の阻害効果をもつ化合物の生成も可能になると予想している。また、このアッセイ系では構造予測がなくてもランダムスクリーニングでも酵素の活性阻害を調べることが可能と判断する。個体でのSHP2変異による活性化を表現型で探ることが可能となった。SHP2のD61G変異体のmRNAインジェクションではNoonan症候群と同様な症状を呈することがわかり、このゼブラフィッシュにSHP2阻害効果がみられた薬剤候補を投与することで個体でのSHP2阻害活性も検討可能になった。個体での阻害薬の効果の判定はマウスや大型動物への投与などの煩雑な過程へのスクリーニング系としても有用であると考えられる。ゼブラフィッシュで効果のないものは、動物投与を行うまでもなく効果が期待できないために、無駄に動物を殺生することなく薬剤の効果判定を行えることになる。

D. 結論

本研究はSHP2阻害薬開発の大きな一歩となる重要なアッセイ系の確立ならびにin silicoのスクリーニングの可能性を示す研究となった。

E. 健健康危険情報

なし

F . 研究発表

（研究業績「英文」）

【原著】

(1) Kawahara A, Nishi T, Hisano Y, Fukui H, Yamaguchi A, and Mochizuki N. The sphingolipid transporter spns2 functions in migration of zebrafish myocardial precursors. **Science** 323: 524-527, 2009

(2) Tabata M, Kadomatsu T, Fukuhara S, Miyata K, Ito Y, Endo M, Urano T, Zhu HJ, Tsukano H, Tazume H, Kaikita K, Miyashita K, Iwawaki T, Shimabukuro M, Sakaguchi K, Ito T, Nakagata N, Yamada T, Katagiri H, Kasuga M, Ando Y, Ogawa H, Mochizuki N, Itoh H, Suda T, Oike Y. Angiopoietin-like protein 2 promotes chronic adipose tissue inflammation and obesity-related systemic insulin resistance. **Cell Metab** 10: 178-188, 2009

(3) Mori M, Nakagami H, Koibuchi N, Miura K, Takami Y, Koriyama H, Hayashi H, Sabe H, Mochizuki N, Morishita R, Kaneda Y. Zyxin mediates actin fiber reorganization in epithelial-mesenchymal transition and contributes to endocardial morphogenesis. **Mol. Biol. Cell** 20: 3115-3124, 2009

(4) Miura K, Nam JM, Kojima C, Mochizuki N, Sabe H. EphA2 Engages Git1 to Suppress Arf6 Activity Modulating Epithelial Cell-Cell Contacts. **Mol. Biol. Cell** 20: 1949-1959, 2009,

(5)Tsuboi S, Takada H, Hara T, Mochizuki N, Funyu T, Saitoh H, Terayama Y, Yamaya K, Ohyama C, Nonoyama S, Ochs HD. FBP17 mediates a common molecular step in the formation of podosomes and phagocytic cups in macrophages. **J. Biol. Chem.** 284: 8548-8556, 2009

(6) Sako K, Fukuhara S, Minami T, Hamakubo T, Song H, Kodama T, Fukamizu A, Gutkind JS, Koh GY, Mochizuki N. Angiopoietin-1 Induces Kruppel-like Factor 2 Expression through a Phosphoinositide 3-Kinase/AKT-dependent Activation of Myocyte Enhancer Factor 2. **J. Biol. Chem.** 284: 5592-5601, 2009

2. 学会発表

特になし。

H. 知的財産権の出願・登録状況

特になし。

別紙4

研究成果の刊行に関する一覧表

雑誌

発表者	論文タイトル	発表誌	巻号	ページ	出版年
Iwata, Y., Katanosaka, Y., Arai, Y., Shigekawa, M., Wakabayashi, S.	Dominant-negative inhibition of Ca^{2+} influx via TRPV2 ameliorates muscular dystrophy in animal models	Hum. Mol. Gen.	18(5)	824-834	2009
Cha ,C.Y., Oka, C., Earm ,Y.E., Wakabayashi S. Noma A.	A Model of Na^+/H^+ Exchanger and Its Central Role in Regulation of pH and Na^+ in Cardiac Myocytes	Biophys J	97(10)	2674-2683	2009
Zanou, N., Iwata, Y., Schakman, O., Lebacq, J., Wakabayashi, S., Gailly, P.	Essential role of TRPV2 ion channel in the sensitivity of dystrophic muscle to eccentric contractions	FEBS Letters	583(22)	3600-3604	2009
T.Kawamura and N.Hirayama	Crystal Structure of Ganciclovir	X-ray Structure Online	25	51-52	2009
F.Anzai,T.Kataishi, T.Nakano, M.Hirayama and N.Hirayama	Crystal Structure of a Novel Diyne, 1,4-Bis(4-((Z)-1-phenyl-2-(trimethylsilyl) vinyl)phenyl)buta-1, 3-diyne	X-ray Structure Analysis Online	25	63-64	2009
T.Kataishi, F,.Anzai,T.Nakano, M.Hirayama and N.Hirayama	Crystal Structure of 1,4-bis[4-((2Z)-(trimeth ylsilyl)-1-phenylethenyl) phenylethynyl]benzene	X-ray Structure Analysis Online	25	111-112	2009
Y.Izuhara, N.Yamaoka, H. Kodama, T. Dan, S.Takizawa, N.Hirayama, K. Meguro, C.van Yperseleide Strihou and T. Miyata	A novel inhibitor of plasminogen activator inhibitor-1 provides antithrombotic benefits devoid of bleeding effect in nonhuman primates	J.Cereb. Blood Flow Metab.	30	1-9	2010
東田欣也、後藤純一、平山令明	疑似分子プローブと標的分子構造に基づく de novo 医薬分子設計法の開発	SAR News	16	16-20	2009

Nakayama D, Ben Ammar, Takeda S.	Crystallization and preliminary X-ray crystallographic analysis of the blood coagulation factor V-activating proteinase (RVV-V) from Russell's viper venom	Acta Cryst	F65	1306-1308	2009
Akiyama, M, Takeda S, Kokame, K, Takagi, J, Miyata, T	Crystal structures of the non-catalytic domains of ADAMTS13 reveal multiple discontinuous exosites for von Willebrand factor	Proc Natl Acad Sci USA	106	19274-19279	2009
Akiyama, M, Takeda S, Kokame, K, Takagi, J, Miyata, T	Production, crystallization and preliminary crystallographic analysis of the exosite-containing fragment of human von Willebrand factor-cleaving proteinase, ADAMTS13	Acta Cryst	F65	739-742	2009
K. Yamada, R. Kuroda, H. Toyakawa, H. Ikeura-Sekiguchi, M. Yasumoto, M. Koike, F. Sakai, K. Mori, H. Mori, N. Fukuyama, E. Sato	A trial for fine and low-dose imaging of biological specimens using quasi-monochromatic laser-Compton X-rays	Nuclear Instruments and Methods in Physics Research	A 608	S7-S10	2009
T. Nishikawa, N. Iwakiri, Y. Kaneko, A. Taguchi, K. Fukushima, H. Mori, N. Morone, J. Kadokawa	Nitric Oxide Release in Human Aortic Endothelial Cells Mediated by Delivery of Amphiphilic Polysiloxane Nanoparticles to Caveolae	Biomacromolecules	10	2074-2085	2009
武田壮一	ADAM ファミリー蛋白質の立体構造と作用機構	蛋白質核酸酵素	54(13)	1754-1759	2009
武田壮一	蛇毒メタロプロテアーゼの立体構造とラッセルクサリヘビ毒素による X 因子活性化機構	血栓止血学会誌	20(3)	307-314	2009
Kawahara A, Nishi T, Hisano Y, Fukui H, Yamaguchi A, and Mochizuki N	The sphingolipid transporter spns2 functions in migration of zebrafish myocardial precursors	Science	323	524-527	2009

Tabata M, Kadomatsu T, Fukuhara S, Miyata K, Ito Y, Endo M, Urano T, Zhu HJ, Tsukano H, Tazume H, Kaikita K, Miyashita K, Iwawaki T, Shimabukuro M, Sakaguchi K, Ito T, Nakagata N, Yamada T, Katagiri H, Kasuga M, Ando Y, Ogawa H, Mochizuki N, Itoh H, Suda T, Oike Y	Angiopoietin-like protein 2 promotes chronic adipose tissue inflammation and obesity-related systemic insulin resistance	Cell Metab.	10	178-188	2009
Mori M, Nakagami H, Koibuchi N, Miura K, Takami Y, Koriyama H, Hayashi H, Sabe H, Mochizuki N, Morishita R, Kaneda Y	Zyxin mediates actin fiber reorganization in epithelial-mesenchymal transition and contributes to endocardial morphogenesis	Mol. Biol. Cell	20	3115-3124	2009
Miura K, Nam JM, Kojima C, Mochizuki N, Sabe H	EphA2 Engages Git1 to Suppress Arf6 Activity Modulating Epithelial Cell-Cell Contacts	Mol. Biol. Cell	20	1949-1959	2009
Tsuboi S, Takada H, Hara T, Mochizuki N, Funyu T, Saitoh H, Terayama Y, Yamaya K, Ohyama C, Nonoyama S, Ochs HD	FBP17 mediates a common molecular step in the formation of podosomes and phagocytic cups in macrophages	J. Biol. Chem.	284	8548-8556	2009
Sako K, Fukuhara S, Minami T, Hamakubo T, Song H, Kodama T, Fukamizu A, Gutkind JS, Koh GY, Mochizuki N	Angiopoietin-1 Induces Kruppel-like Factor 2 Expression through a Phosphoinositide 3-Kinase/AKT-dependent Activation of Myocyte Enhancer Factor 2	J. Biol. Chem.	284	5592-5601	2009

Copy Edited by: WP

Human Molecular Genetics, 2008, Vol. 18, No. ? **1–11**
doi:10.1093/hmg/ddn408
Advance Access published on xxx

Dominant-negative inhibition of Ca^{2+} influx via TRPV2 ameliorates muscular dystrophy in animal models

Yuko Iwata[1,*], Yuki Katanosaka[1], Yuji Arai[2], Munekazu Shigekawa[1,†] and Shigeo Wakabayashi[1]

[1]Department of Molecular Physiology and [2]Department of Bioscience, National Cardiovascular Center Research Institute Suita, Osaka 565-8565, Japan

Received August 19, 2008; Revised and Accepted December 1, 2008

Muscular dystrophy is a severe degenerative disorder of skeletal muscle characterized by progressive muscle weakness. One subgroup of this disease is caused by a defect in the gene encoding one of the components of the dystrophin–glycoprotein complex, resulting in a significant disruption of membrane integrity and/or stability and, consequently, a sustained increase in the cytosolic Ca^{2+} concentration ($[Ca^{2+}]_i$). In the present study, we demonstrate that muscular dystrophy is ameliorated in two animal models, dystrophin-deficient *mdx* mice and δ-sarcoglycan-deficient BIO14.6 hamsters by dominant-negative inhibition of the transient receptor potential cation channel, TRPV2, a principal candidate for Ca^{2+}-entry pathways. When transgenic (Tg) mice expressing a TRPV2 mutant in muscle were crossed with *mdx* mice, the $[Ca^{2+}]_i$ increase in muscle fibers was reduced by dominant-negative inhibition of endogenous TRPV2. Furthermore, histological, biochemical and physiological indices characterizing dystrophic pathology, such as an increased number of central nuclei and fiber size variability/fibrosis/apoptosis, elevated serum creatine kinase levels, and reduced muscle performance, were all ameliorated in the *mdx*/Tg mice. Similar beneficial effects were also observed in the muscles of BIO14.6 hamsters infected with adenovirus carrying mutant TRPV2. We propose that TRPV2 is a principal Ca^{2+}-entry route leading to a sustained $[Ca^{2+}]_i$ increase and muscle degeneration, and that it is a promising therapeutic target for the treatment of muscular dystrophy.

INTRODUCTION

Muscular dystrophy is a heterogeneous genetic disease that causes severe skeletal muscle degeneration characterized by fiber weakness and muscle fibrosis, severe local inflammation and, at least initially, muscle regeneration. A subset of muscular dystrophy is caused by a mutation in the gene encoding one of the components of the dystrophin–glycoprotein complex (DGC) (1–3), a multi-subunit complex (2,4,5) that spans the sarcolemma to structurally link the extracellular matrix and actin cytoskeleton (6). Therefore, disruption of the DGC could significantly disrupt membrane integrity or stability during muscle contraction and relaxation and prevent myocyte survival. The enhanced susceptibility to exercise-induced muscle fiber damage is observed in dystrophic animals, such as δ-sarcoglycan (SG)-deficient BIO14.6 hamsters and dystrophin-deficient *mdx* mice, which are genetic homologues of human limb-girdle and Duchenne muscular dystrophy (DMD), respectively.

Although many studies have molecularly characterized the genes responsible for and the histological pathology of dystrophic tissues, little is known about the pathways by which the genetic defects lead to muscle degeneration. A number of studies have reported the chronic elevation of the cytosolic Ca^{2+} concentration ($[Ca^{2+}]_i$) beneath the sarcolemma or within other cell compartments of skeletal muscle fibers, or in cultured myotubes from dystrophin-deficient DMD patients and *mdx* mice. Increased $[Ca^{2+}]_i$ could activate Ca^{2+}-dependent proteases and promote protein degradation and cell necrosis (7–9). Several pathways leading to an increase of the $[Ca^{2+}]_i$ have been suggested to be involved in the pathology of muscular dystrophy (10–15). We previously identified a stretch-activated channel, the transient receptor potential (TRP) cation channel

*To whom correspondence should be addressed at: Department of Molecular Physiology, National Cardiovascular Center Research Institute, Fujishiro-dai 5-7, Suita, Osaka 565-8565, Japan. Tel: +81 668335012; Fax: +81 668355314; Email: yukoiwat@ri.ncvc.go.jp
†Present address: Department of Human Life Science, Senri Kinran University, Suita, Osaka 565-0873, Japan.

© *The Author 2008. Published by Oxford University Press. All rights reserved.*
For Permissions, please email: journals.permissions@oxfordjournals.org

TRPV2, that may function in the pathogenesis of myocyte degeneration caused by DGC disruption (16). The TRP channels form a large family of cation channels that likely function as tetramers in various processes, such as sensory signaling (17–19). The cellular function of TRPV2, however, remains to be characterized. We previously found that TRPV2 normally localizes in the intracellular membrane compartments but translocates to the plasma membrane in dystrophic muscle fibers, thus contributing to a sustained $[Ca^{2+}]_i$ increase (16).

To determine the relationship between TRPV2 activation and muscle degeneration, and determine whether TRPV2 inhibition potentially prevents muscular dystrophy, we introduced mutant TRPV2 into dystrophic muscles to inhibit endogenous TRPV2 activity via a dominant-negative effect. Here we report that transgenic (Tg) or adenoviral expression of dominant-negative TRPV2 ameliorates muscle pathology in *mdx* mice and BIO14.6 hamsters by preventing abnormal Ca^{2+} handling.

RESULTS

Characterization of dominant-negative TRPV2 mutants

Conserved acidic residues in the putative pore region of TRP cation channels are known to be crucial for cation permeation (20,21). We generated three TRPV2 mutants by substituting two highly conserved glutamate residues (Glu594 and Glu604) in the putative pore region with lysine, either individually (E594K and E604K) or together (DK). The TRPV2 mutants were stably expressed in Chinese hamster ovary (CHO) cells, as confirmed by immunoblot, which showed two protein bands with different degrees of glycosylation (Fig. 1B). The immunofluorescence of TRPV2 expressed in CHO cells revealed that, in the absence of serum, most TRPV2 was localized in the intracellular membrane compartments (Fig. 1C). In contrast, upon stimulation with serum, a portion of TRPV2 translocated to the surface membranes (Fig. 1C) as previously reported (22). Interestingly, a similar serum-induced translocation occurred with the three TRPV2 mutants (Fig. 1C, data not shown for E594K and DK).

We next assessed TRPV2 activity by measuring the Ca^{2+}-induced change of the $[Ca^{2+}]_i$ by ratiometric scanning of the fura-2 fluorescence. As shown in Fig. 1D, the perfusion of cells with a 2 mM $CaCl_2$ solution resulted in a rapid and large increase in the $[Ca^{2+}]_i$ of cells expressing wild-type TRPV2 compared to non-transfected control cells (Supplementary Material, Fig. S1). In contrast, the increase in $[Ca^{2+}]_i$ did not occur in cells expressing E604K (Fig. 1D) or the other two mutants (Fig. 1E), suggesting that these mutations abolished Ca^{2+}-permeation via TRPV2. Because the TRP channel family likely functions as tetramers (17,18), we predicted that the TRPV2 mutants would have a dominant-negative effect on wild-type TRPV2 activity. We transiently transfected green fluorescent protein (GFP)-tagged TRPV2 mutants in cells stably expressing wild-type TRPV2 and measured the $[Ca^{2+}]_i$ in GFP-positive cells (Supplementary Material, Fig. S1). Transfection with the mutants dramatically diminished the Ca^{2+}-induced rise (Fig. 1F), suggesting that the TRPV2 mutants exerted a strong dominant-negative effect. Similar inhibitory effects of the mutants were also observed in HEK293 cells when the $[Ca^{2+}]_i$ increase was induced with high Ca^{2+} solution or the TRPV channel agonist 2-aminoethoxydiphenyl borate (2-APB) (Supplementary Material, Fig. S2). Wild-type and mutant TRPV2 were co-localized in the plasma membranes of HEK293 cells (Supplementary Material, Fig. S2). Furthermore, surface biotinylation and co-immunoprecipitation assays revealed that mutant TRPV2 is capable of forming oligomers with wild-type TRPV2 in the cell surface (Supplementary Material, Fig. S3).

Transgenic expression of dominant-negative TRPV2 blocks abnormal Ca^{2+} handling in *mdx* mice

To assess the relationship between TRPV2 activation and muscle degeneration, we analyzed whether the expression of dominant-negative TRPV2 prevents muscle damage in dystrophin-deficient *mdx* mice. We first generated transgenic mice (C57/BL6J background) expressing the hemaglutinin (HA)-tagged E604K (E604K-HA) mutant under the control of the α-skeletal actin promoter in skeletal muscle. Two lines of male Tg mice were then crossed with female *mdx* mice, and because muscular dystrophy is X-linked recessive in *mdx* mice, the resulting male mice were predicted to express the E604K-HA mutant and be deficient in dystrophin. The expression of the E604K-HA mutant was confirmed by anti-HA immunoblotting only in the Tg and *mdx*/Tg mice, although only half level of E604K-HA expression was detected in the latter mice as expected from heterozygotes (Fig. 2A). Interestingly, the level of endogenous TRPV2 was elevated by approximately 2-fold in *mdx* mice compared to controls, but TRPV2 levels were reduced in the *mdx*/Tg mice (Fig. 2A). While endogenous TRPV2 was broadly distributed in the skeletal muscle of control mice (Fig. 2Ba), it almost exclusively localized in the sarcolemma of *mdx* muscles (Fig. 2Bb). On the other hand, exogenous E604K-HA was mostly observed in the intracellular membranes, although a small portion was localized in the sarcolemma (Fig. 2Bg and h). In addition, the expression of E604K-HA reduced the sarcolemmal localization of endogenous TRPV2 in *mdx* muscles (Figs 2Bc and 3Ad, also see Supplementary Material, Fig. S4).

We isolated the Flexor digitorum brevis (FDB) fibers from each mouse and immunostained with the anti-TRPV2 antibody, revealing that, consistent with immunostaining in muscle sections, most TRPV2 localized in the sarcolemma of *mdx* fibers (Fig. 3Ab), but not in the fibers from wild-type mice (Fig. 3Aa); this sarcolemmal localization was much lower in the *mdx*/Tg mice (Fig. 3Ad). Consistent with the sarcolemmal localization of TRPV2 in *mdx* fibers, the perfusion of fibers with 2-APB induced a large and rapid increase in $[Ca^{2+}]_i$ in fibers from *mdx* mice, which was completely inhibited by the TRPV channel antagonist ruthenium red (Fig. 3B). An increase in $[Ca^{2+}]_i$ was also observed to occur upon perfusion with high Ca^{2+} solution (2–5 mM, see Fig. 3B and Supplementary Material, Fig. S5). These Ca^{2+} increases were reduced in fibers from *mdx*/Tg mice (Fig. 3B–D and Supplementary Material, Fig. S5), suggesting that the introduction of E604K-HA inhibited Ca^{2+}-entry via endogenous TRPV2. Since TRPV2 is a stretch-activated channel, we analyzed the effect of mechanical stress on membrane deformation of isolated fibers. We observed that hypo-osmotic stress (70% osmolarity) resulted in severe damage in fibers from *mdx*

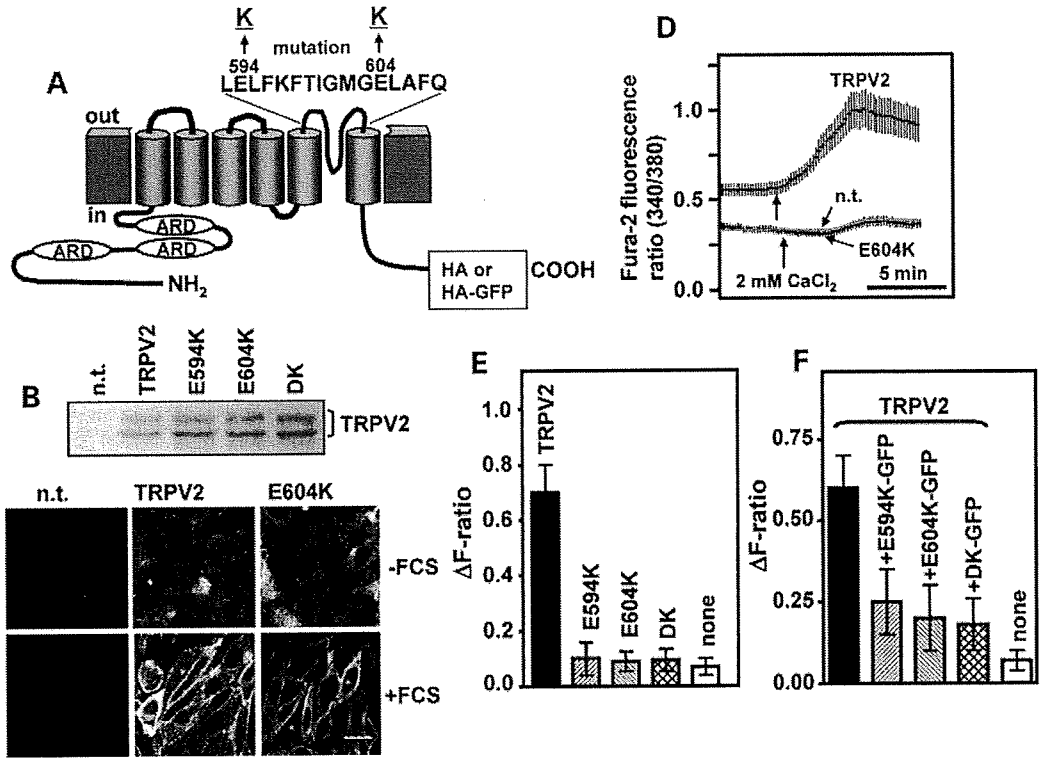

Figure 1. Dominant-negative mutants of TRPV2. (**A**) A schematic drawing of TRPV2 constructions. The C-terminus of TRPV2 was tagged with either the HA-epitope alone or with GFP inserted after the HA-tag. Conserved residues in the putative pore region (Glu594 and Glu604) were substituted with lysine, either individually or together. ARD, ankyrin repeat domain. (**B**) Equal amounts (10 μg) of lysate from CHO cells stably expressing wild-type or mutant TRPV2 were subjected to immunoblot analysis using anti-TRPV2 antibody. (**C**) Immunohistochemical analysis. Cells expressing wild-type TRPV2 or E604K-HA were serum-depleted overnight (−FCS, upper panel); stimulated for 15 min with 10% serum (+FCS, lower panel) and fixed, permeabilized and immunostained with anti-TRPV2 antibody. n.t., no transfection. Scale bar: 50 μm. (**D**) Typical traces from the ratiometric scanning of fura-2 fluorescence. Transfected or non-transfected (n.t., *grey*) cells were placed on glass coverslips and perfused with solution containing 0.5 mM $CaCl_2$. Perfusion with high concentrations of $CaCl_2$ (2 mM) resulted in a rapid increase in the fluorescence ratio in TRPV2-transfectants, but not E604K-HA. (**E**) Summary of fura-2 fluorescence data. The ΔF ratio was calculated by subtracting the resting level of the fluorescence ratio from the maximal level after high Ca^{2+} addition. (**F**) The GFP-tagged TRPV2 constructs were transiently expressed in TRPV2 stable transfectants and the fluorescence data from GFP-positive cells were summarized. Values are means ± SD of more than 20 cells (E and F).

mice, but not much in fibers from *mdx*/Tg mice. Bleb formation in *mdx* fibers was inhibited by more than 60% upon expression of E604K-HA (data not shown). A sustained increase in $[Ca^{2+}]_i$ via surface TRPV2 would result in various phenotypic changes in the skeletal muscles of *mdx* mice via activation of Ca^{2+}-dependent enzymes. Consistent with this idea, the phosphorylation of Ca^{2+}/calmodulin-dependent protein kinase (CaMK)II was significantly higher in *mdx* skeletal muscle compared to controls (Fig. 2A). In contrast, phosphorylated CaMKII was markedly reduced in the *mdx*/Tg mice (Fig. 2A), suggesting a reduced $[Ca^{2+}]_i$ in muscle fibers from these mice.

Transgenic expression of dominant-negative TRPV2 ameliorates muscular dystrophy in *mdx* mice

To determine whether dominant-negative inhibition of TRPV2 could prevent muscular dystrophy, we first analyzed the overall symptoms for muscle degeneration. Expression of E604K-HA in *mdx* mice (*mdx*/Tg) markedly (40–60%) reduced the level of serum creatine kinase (CK), a marker for muscle damage (Fig. 4A), and improved muscle performance as evaluated by a grip test (50–70% of wild-type) (Fig. 4B). The improvement of muscle damage was observed in *mdx*/Tg mice produced from two Tg lines (I and II).

We next analyzed the histological characteristics of skeletal muscles. Skeletal muscle-specific expression of E604K-HA produced no striking morphological changes in the muscles of Tg mice (Fig. 5Ab), and muscle fibers from *mdx*/Tg mice (Fig. 5Ad and f) presented with a healthier appearance compared to their *mdx* counterparts (Fig. 5Ac and e). Among several abnormal morphological indices, dystrophic muscle fibers are known to display a greater variation in their cross-sectional area (23). Muscles from *mdx*/Tg mice exhibited a greater homogeneity compared to *mdx* mice in respect to fiber size variability, determined by averaging the standard deviation of the cross-sectional areas (Fig. 5B). Furthermore, the expression of E604K-HA reduced (60% reduction) the number of fibers with central nuclei (Fig. 5C) in 10 week *mdx*/Tg mice, the area of inflammatory infiltrate (more than 90% reduction) and Evans blue dye (EBD) uptake (marker of membrane integrity, 80% reduction) (Fig. 5D) in similar-aged

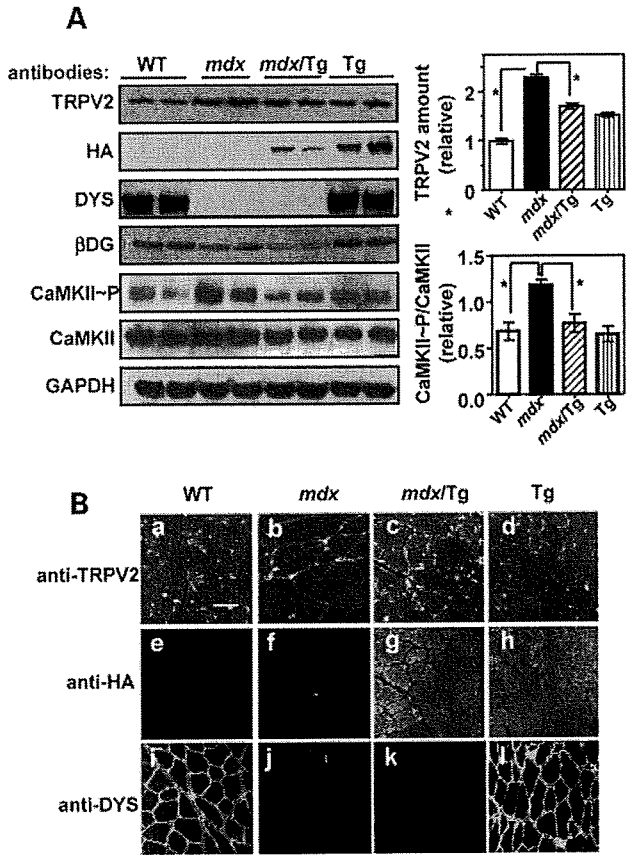

Figure 2. Protein expression pattern in wild-type, *mdx*, Tg and *mdx*/Tg mice. (**A**) Immunoblot analysis with indicated antibodies. The relative amount of TRPV2 was normalized to GAPDH, and phosphorylated CaMKII (CaMKII-P) was normalized to the total amount of CaMKII (right panels). (**B**) Immunohistochemical analysis of TRPV2 and dystrophin in frozen cross sections of skeletal muscle. Double immunostaining was performed using FITC-conjugated rat anti-HA (e–h) and rabbit anti-TRPV2 (a–d) followed by rhodamine-conjugated secondary antibodies. Immunostaining was also performed with anti-dystrophin (i–l) antibody. Surface localization of TRPV2 in *mdx* mice was reduced by crossing with Tg mice (*mdx*/Tg). See Supplementary Material, Fig. S4 for a semi-quantitative analysis. Scale bar: 50 μm.

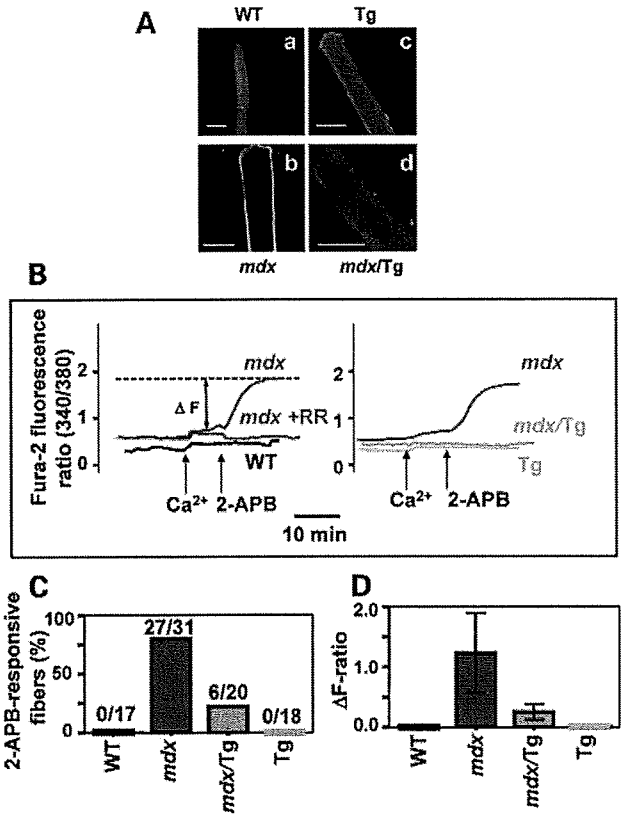

Figure 3. Dominant-negative TRPV2 inhibits a Ca^{2+} abnormality in *mdx* mice. (**A**) FDB muscle fibers isolated from wild-type (a), *mdx* (b), Tg (c) and *mdx*/Tg (d) mice were visualized by immunofluorescence staining with anti-TRPV2 antibody (a–d). Scale, 100 μm. (**B**) Representative traces for the 2-APB-induced increase in the fura-2 fluorescence ratio. Fibers placed in a solution containing 2 mM $CaCl_2$ were stimulated with high Ca^{2+} (5 mM, indicated by arrow) and then 500 μM 2-APB. Ruthenium red was included just in the 2-APB solution (blue line). The Ca^{2+} increase induced by 2-APB was reduced in *mdx*/Tg fibers and completely blocked by ruthenium red (40 μM). (**C**) The ΔF ratio was calculated by subtracting the resting fluorescence ratio from the maximal ratio after inclusion of 2-APB. Fibers exhibiting a ΔF-ratio >0.3 were defined as 2-APB-responsive fibers and plotted. The values for 2-APB-responsive fibers per total number of analyzed fibers from each of 3–4 mice are shown. (**D**) The ΔF-ratio was averaged and plotted (means ± SD).

mice, suggesting that the degeneration of myofibers markedly decreased and subsequent muscle regeneration was reduced in the *mdx*/Tg mice. In addition, Masson's trichrome staining revealed that the foci of fibrosis, reflecting the progressive replacement of myofibers with connective tissue, was frequently detected in *mdx* mice, but the expression of E604K-HA reduced fibrosis more than 60% (Fig. 5E and F). The high level of apoptosis seen in *mdx* muscle was also reduced in *mdx*/Tg muscle (Fig. 5G and H). We observed that the expression of E604K-HA may be somewhat mosaic in *mdx*/Tg muscle as well as Tg muscle as seen in Fig.2Bg and h, thus exerts a different dominant-negative effect on individual muscle fibers. In order to directly check the involvement of this E604K-HA expression, we compared the area stained with incorporated EBD, a marker of cell injury, to the area immunostained with anti-HA or anti-TRPV2 using serial sections (Supplementary Material, Fig. S6). Fibers stained with EBD, which were sometimes observed in *mdx*/Tg mice, corresponded to those showing relatively low expression level of E604K-HA, but the condensed expression of endogenous TRPV2 (Supplementary Material, Fig. S6C). Thus, high membrane expression of endogenous TRPV2 well correlates with pronounced EBD uptake. Taken together, these data suggest that the inhibition of TRPV2 significantly improves muscular dystrophy in *mdx* mice, and TRPV2 may play a pivotal role in causing dystrophic muscle damage.

Adenoviral expression of dominant-negative TRPV2 ameliorates muscular dystrophy in BIO14.6 hamsters

We next examined whether the inhibition of TRPV2 also reduces muscle damage in BIO14.6 hamster, another model of dystrophy. Infection of cultured BIO14.6 myotubes with

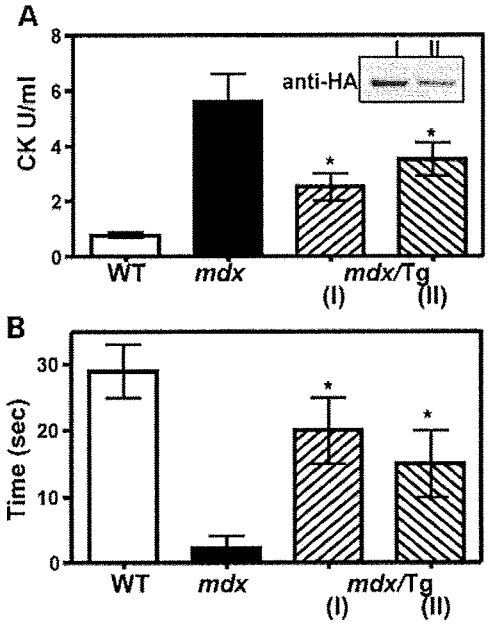

Figure 4. Dominant-negative TRPV2 ameliorates muscle dysfunction in *mdx* mice. (**A**) Serum creatine kinase (CK) levels were compared among 5–10 week old wild-type, *mdx* and *mdx*/Tg mice produced from Tg lines I and II, respectively. Data are means ± SD of 6–21 mice. Protein expression levels of E604K-HA in *mdx*/Tg mice from two Tg lines examined by immunoblot analysis with anti-HA antibody (A inset). (**B**) Muscle function evaluated by grip test in 5–10 week old wild-type, *mdx* and *mdx*/Tg mice produced from Tg lines I and II, respectively. Data are means ± SD of 6–21 mice.

adenovirus carrying DK-HA resulted in the expression of HA-tagged TRPV2 mutant (Fig. 6A). While endogenous TRPV2 was almost exclusively localized in sarcolemma of BIO14.6 myotubes (Fig. 6A and B), upon expression of DK-HA it was translocated from the surface to the intracellular membranes of myotubes, where endogenous and exogenous TRPV2 proteins appeared to be co-localized (Fig. 6Ac). We found that the Ca^{2+}-induced increase in the $[Ca^{2+}]_i$ was markedly suppressed in myotubes infected with adenovirus carrying DK-HA (Fig. 6B). In addition, adenovirally expressed DK-HA reduced the stretch-induced CK release observed in control BIO14.6 myotubes (Fig. 6C), suggesting that the inhibition of TRPV2 is effective for reducing the stretch-induced cell damage to BIO14.6 myotubes. Of note, upon infection of adenovirus, total level of TRPV2 expression does not increase so much, whereas DK-HA is successfully expressed in myotubes (Fig. 6A), suggesting that the exogenous expression of DK-HA may inhibit the expression of endogenous TRPV2. However, the expression of DK-HA clearly changed the distribution pattern of endogenous TRPV2 and suppressed Ca^{2+} abnormality, suggesting that the expression level of DK-HA would be sufficient to affect the function of endogenous TRPV2.

Furthermore, we injected adenovirus carrying β-gal or DK-HA into the quadriceps of 60-day-old BIO14.6 hamsters. Treatment of muscles with adenovirus carrying DK-HA resulted in the expression of HA-tagged TRPV2 mutant (upper panel of Fig. 7A) and reduction in plasma membrane localization of TRPV2 (lower panel of Fig. 7A). Fourteen days later, the muscle degeneration was reduced in DK-HA virus-infected BIO14.6 hamsters compared to those infected with adenoviral β-gal (Fig. 7Ba and b). The number of central nuclei and fiber size variability was reduced (40–50%) upon DK-HA infection (Fig. 7C), and TUNEL staining additionally revealed a marked reduction (~80%) in apoptosis in DK-HA-infected muscles (Fig. 7Bc and d, and C). Together, these data demonstrate that, similar to the *mdx* mouse model, the inhibition of TRPV2 is capable of greatly ameliorating muscular dystrophy in the BIO14.6 hamster model.

DISCUSSION

Abnormal Ca^{2+}-handling is a hallmark of muscle dysfunction in muscular dystrophy. In the present study, we demonstrated that the Tg or adenoviral expression of mutant TRPV2 reduces the $[Ca^{2+}]_i$ increase and muscle degeneration, and ameliorated muscle dystrophy, in the *mdx* mouse and BIO14.6 hamster models *in vivo* and *in vitro*. We presented evidence that the beneficial effect of mutant TRPV2 is due to the dominant-negative inhibition of endogenous TRPV2, resulting in suppressed Ca^{2+}-permeation and reduced plasma membrane expression. In addition to the decreased Ca^{2+} influx in isolated FDB fibers, we observed that the enhanced phosphorylation of CaMKII in *mdx* mice was reduced after crossing them with Tg mice, strongly suggesting that the increase in intracellular Ca^{2+} level was indeed reduced in the skeletal muscle of *mdx*/Tg mice. This inhibition likely occurs from the oligomerization of the mutant subunit with endogenous TRPV2 subunits upon assembly of TRPV2 channels because TRPV2 is thought to function as a homo-oligomer (17,18,24). In fact, this is supported by the finding that the subcellular localization of endogenous TRPV2 is markedly affected by the exogenous expression of mutant TRPV2 in *mdx*/Tg mice. Although a recent study reported that TRPV2 may also be capable of forming hetero-oligomers with TRPV1 and/or TRPV3 (25), the expression of TRPV1 and TRPV3 was not detected by immunoblot analysis in mouse skeletal muscle (Supplementary Material, Fig. S7). On the other hand, the TRPC family has been reported to be involved in abnormal Ca^{2+} handling in the skeletal muscle of *mdx* mice (14). However, we observed that the $[Ca^{2+}]_i$ was increased by 2-APB, a TRPC channel antagonist (26). Furthermore, a significant difference was not observed in the expression of TRPC family members (TRPC1, 3, 4 and 6) among four kinds of mice (Supplementary Material, Fig. S7). Therefore, the involvement of TRPC channels would be minor. Thus, our present data, together with previous data (16), strongly suggest that TRPV2 plays a crucial pathological role in the Ca^{2+}-induced muscle degeneration of dystrophic muscles.

Our findings also provide convincing validation of the therapeutic potential of TRPV2 for muscular dystrophy. This protein has several advantages as a therapeutic target. First, most TRPV2 localizes to the intracellular membranes in normal, healthy skeletal muscle, but it translocates to the surface membrane upon muscle degeneration (16); hence, specific inhibitors against TRPV2 are predicted to only act

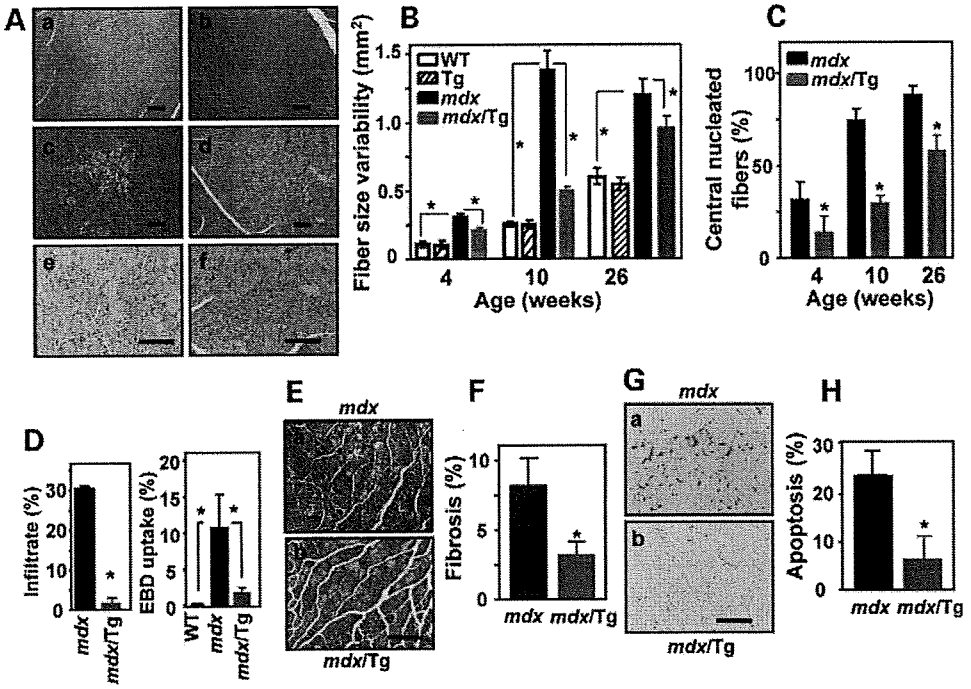

Figure 5. Dominant-negative TRPV2 attenuates muscle degeneration in *mdx* mice. (**A**) Representative images for H&E staining of quadricep sections from wild type (a), Tg (b), *mdx* (c and e) and *mdx*/Tg (d and f) mice. (a–d) Twenty-six weeks old, (e and f) 10 weeks old. Scale, 100 μm. (**B–D**) Histological parameters were measured using H&E stained sections. Sections covering more than 1000 fibers from three to four mice were used for an analysis of each group. Cross-sectional areas of each individual fiber were measured and the variability of muscle fiber size was determined by averaging the standard deviations of data (B). The number of centrally nucleated fibers (C) was also measured using the same histological sections. (D) Percentage of inflammatory infiltration area measured using the histological sections from 7 to 10 week old *mdx* and *mdx*/Tg (line I) mice. Data are means ± SD of four mice. The percentage of EBD-positive area (cf. Supplementary Material, Fig. S6). Data are means ± SD of four mice. (**E** and **F**) Masson's trichrome staining of 26 week old *mdx* (a) and *mdx*/Tg (b) mice, and measurements of the area of fibrosis. (**G** and **H**) TUNEL labeling of sections of gastrocnemius muscle samples from 10 week old *mdx* (a) or *mdx*/Tg (b) mice, and the number of fibers exhibiting apoptosis. For histological analysis, sections covering more than 1000 fibers from three to four mice were used for measurements. Scale bar, 100 μm.

on degenerative muscles. Second, surface translocation and the subsequent activation of TRPV2 may occur in a wide range of genetic or non-genetic muscle diseases (16). For example, we recently observed that the surface translocation of TRPV2 also occurs in the hearts of idiopathic cardiomyopathy patients (unpublished observation). Thus, specific inhibitors against TRPV2 could be potentially useful for the treatment of various degenerative muscle diseases.

In this study, we presented evidence that the inhibition of TRPV2 is able to ameliorate several indices characterizing the dystrophic pathology. However, it is important to consider that the pathology of dystrophin-deficient muscles covers a broader area that includes susceptibility to exercise-induced injury, oxidative stress and an impaired regenerative capacity. We observed that the inhibition of TRPV2 resulted in a different degree of amelioration in dystrophic indices examined in this study, reflecting the complexity of this disease. For example, good amelioration (60–90%) was seen in all dystrophic parameters in young *mdx*/Tg mice (4–10 weeks), but in old mice (more than 26 weeks) only 30–40% amelioration was seen in fiber size variability and in number of centrally nucleated fibers, although fibrosis was markedly reduced even in old mice. In young *mdx*/Tg mice, it is likely that dominant-negative TRPV2 decreases the susceptibility of dystrophic muscles to the on-going cycles of degeneration and regeneration induced by contraction, while in older mice such a cycle may be saturated and no more changed. Thus, the inhibition of TRPV2 appears to primarily promote the retardation of muscle degeneration onset. Furthermore, we observed a partial amelioration (40–60%) of serum CK levels, when compared with apparently better improvement of tissue injury in limbs muscles such as quadriceps examined. This would be due to the fact that serum CK levels reflect the overall state of all muscles including diaphragm and back muscle not examined in this study. Although dominant-negative TRPV2 does not completely prevent dystrophic pathology, our present data suggest that TRPV2 would be a key molecule to link the disruption of DGC with muscle degeneration.

An important issue is the molecular mechanism by which TRPV2 translocates to the plasma membrane and becomes activated in dystrophic muscles. In both *mdx* and *mdx*/Tg mice, it is likely that the muscles are subjected to continuous mechanical stress caused by the dystrophin deficiency. Such mechanical stretch may enhance the secretion of various hormones or bioactive substances, which potentially promote TRPV2 translocation via receptor stimulation because translocation is known to occur in response to various signals,

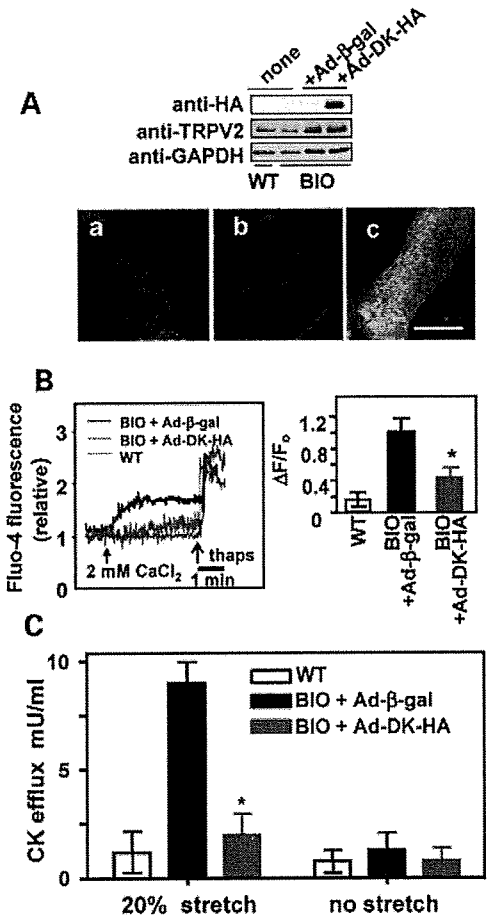

Figure 6. Adenoviral dominant-negative TRPV2 improves abnormal Ca^{2+} handling and muscle degeneration in cultured myotubes from BIO14.6 hamsters. (**A**) Immunoblot analysis of wild-type (lane 1) and BIO14.6 myotubes (lanes 2–4) infected with Ad-β-gal (lane 3) or Ad-DK-HA (lane 4) for expressed mutant TRPV2 (DK-HA), total TRPV2 and GAPDH (anti-GAPDH antibody). Lower panel: immunocytochemistry of TRPV2 in cultured myotubes. Myotubes from wild-type (a) and BIO14.6 infected with Ad-β-gal (b) were immunostained with anti-TRPV2. BIO 14.6 myotubes infected with Ad-DK-HA were double-stained with anti-TRPV2 (red) and anti-HA (green), and then two images were merged. (**B**) Typical trace of the extracellular Ca^{2+}-induced change in fluo-4 fluorescence in wild-type (blue line) or BIO14.6 myotubes infected with Ad-β-gal (black line) or Ad-DK-HA (red line). thaps, thapsigargin. External Ca^{2+}-induced maximal fluorescence increments were normalized by the initial value ($\Delta F/F_0$). (**C**) Wild type or adenovirus-infected BIO14.6 myotubes were subjected to 20% elongation 1 h and the level of CK released to the medium was measured.

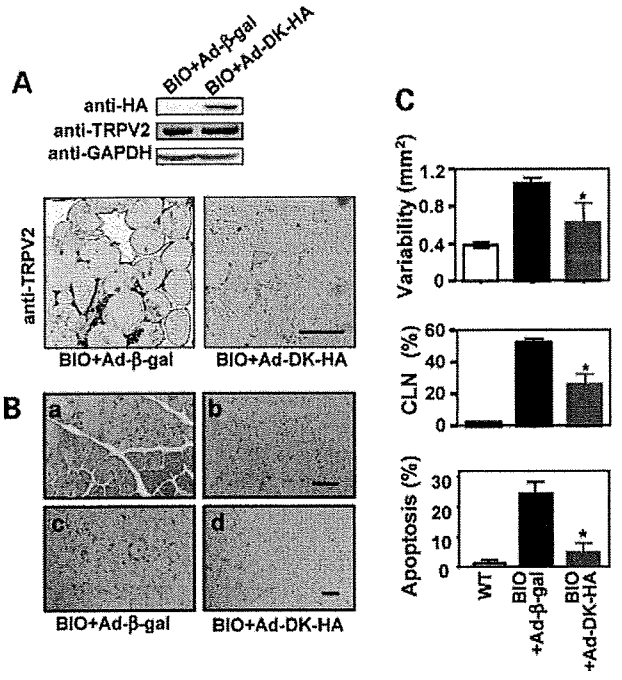

Figure 7. Adenoviral dominant-negative TRPV2 ameliorates muscular dystrophy of skeletal muscle from BIO14.6 hamsters. (**A**) Immunoblot analysis of BIO14.6 hamster skeletal muscles which were intramuscularly injected with adenovirus carrying β-gal (lane 1) or DK-HA (lane 2). Sections of BIO14.6 hamster skeletal muscles injected with adenovirus carrying β-gal (left) or DK-HA (right) were stained with anti-TRPV2. Scale bar: 100 μm. (**B**) Skeletal muscles were stained with H&E (upper panels) or TUNEL (lower panels). Scale bar: 100 μm. (**C**) Cross-sectional areas of each individual fiber were measured and the variability of muscle fiber size was determined by averaging the standard deviations of data (upper). The number of centrally nucleated fibers was also measured using the same histological sections (middle). Number of apoptotic fibers is shown as a ratio between TUNEL labeled nuclei and total nuclei (>1000) observed in three hamsters (lower).

such as growth factors and chemotactic peptides (16,22,27). We recently reported that stretch-induced ATP release contributes to abnormal Na^+ and Ca^{2+} handlings in dystrophic muscles via the P2 receptor (28). In addition, the release of hormones such as IGF-1 and TGFβ has been well documented in dystrophic pathogenesis (28–30). The stretch signal is expected to be generated in both *mdx* and *mdx*/Tg mice. However, unexpectedly, dominant-negative TRPV2 markedly inhibited the plasma membrane retention of TRPV2 in *mdx*/Tg muscle fibers (see Figs 2B and 3A and Supplementary Material, Fig. S4 and S6), suggesting that TRPV2 activity may be required for surface localization in *mdx* muscles. In fact, we have previously shown that the removal of extracellular Ca^{2+} or stretch-activated channel inhibitor Gd^{3+} and general TRPV inhibitor ruthenium red markedly promote the internalization of TRPV2 in dystrophic myotubes (16). It is likely that the increase in local Ca^{2+} levels mediated by TRPV2 contributes to the persistent plasma membrane retention of TRPV2 in dystrophic muscles by blocking their internalization. In this regard, a recent study reported that TRPV2 may function as an endosomal Ca^{2+} release channel, which would control endosome fusion and/or endocytosis (31). Understanding the molecular mechanism of TRPV2 recycling will require further investigation and may accelerate the development of novel therapeutic strategies towards TRPV2.

We observed that the expression of dominant-negative TRPV2 itself exerts no apparent detrimental effect on the function and histological characteristics of muscles in Tg mice, suggesting a minor physiological role of TRPV2 in skeletal muscle. On the other hand, we presented evidence that TRPV2 can provide a Ca^{2+} pool, leading to the activation of CaMKII in *mdx* mice. Since the CaMKII-induced phosphorylation of histone deacetylase, together with the calcineurin/NFAT pathway, is known to

be critical for inducing skeletal muscle remodeling (32), TRPV2 may also play an important physiological role in Ca^{2+}-dependent remodeling processes during muscle injury and/or exercise. Although we do not exclude such a possible physiological role, the present findings suggest that activated TRPV2 becomes a major risk factor in dystrophic muscles.

In conclusion, the specific inhibition of TRPV2 led to a significant amelioration of muscle pathology in dystrophic animal models, and this channel is a promising therapeutic target for muscular dystrophy.

MATERIALS AND METHODS

Antibodies

Affinity-purified rabbit polyclonal anti-TRPV2 antibody was described previously (16). Other antibodies were obtained from the following sources: mouse monoclonal anti-glyceraldehyde-3-phosphate-dehydrogenase (GAPDH), rabbit polyclonal anti-TRPV1, Chemicon; mouse monoclonal anti-dystrophin, Sigma; rat anti-HA antibody (3F10), Roche; rabbit anti-GFP, Medical & Biological Laboratories co., LTD; mouse monoclonal anti-β-dystroglycan, Novocastra Laboratories, Newcastle, UK; rabbit polyclonal anti-CaMKII and anti-TRPV3, Santa Cruz Biotechnology, INC; mouse monoclonal anti-phosphorylated CaMKII, ABR Golden Co.; rabbit polyclonal anti-TRPCs (TRPC1, 3, 4 and 6)and anti-TRPV4, Alomone labs Ltd.

DNA manipulation and adenovirus production

All plasmid constructions of TRPV2 were essentially carried out by PCR-based strategy using the full-length mouse TRPV2 cDNA cloned into the pIRES expression vector (Invitrogen, Carlsbad, CA, USA). In some constructs, a HA-tag or GFP was cloned to the C-terminus of TRPV2 in pIRES or pEGFP-N1 (Clontech, Palo Alto, CA, USA) vector, respectively. GFP was inserted at the C-terminus just after the HA-tag. Three mutants were produced by substituting the conserved Glu residues (Glu594 and Glu604) of TRPV2 with Lys, either singly (E594K or E604K) or together (DK). For adenoviral gene transfer, we inserted the TRPV2 mutant cDNAs or β-gal as a control into the Adeno-X^{TM} viral vector (Clontech). Adenovirus was produced according to the manufacturer's protocol. One-day-old myotubes in differentiated medium were infected with adenoviruses at an MOI of 5–10 viral particles per cell for 24 h and cultured for an additional 36–48 h. For *in vivo* experiments, a virus aliquot was injected into right quadriceps at 5×10^9 *pfu*. Fourteen days after injection, the hamsters were subjected to experiments.

Transgenic mice

The transgene was constructed by inserting a cDNA encoding the full-length mouse TRPV2 mutant tagged with HA (E604K-HA) into the cloning site between the human α-skeletal actin promoter and the SV40 polyadenylation sequence of the plasmid [kindly provided by Dr Jeffrey S. Chamberlain (33)]. The transgene was used to generate Tg mice from C57BL/6J mice according to standard procedures. Two lines (I and II) of male F2 transgenic homozygotes were mated with female *mdx* mice. Male pups that expressed transgene were identified through PCR screening of genomic DNA extracted from tail tissue. Only the male *mdx*/Tg offspring (*mdx*/Tg I or II) were analyzed. The absence of dystrophin from these mice was confirmed by immunological detection with anti-dystrophin antibody. Genotyping was carried out by PCR with specific primers. PCR of the tail DNA was used to identify Tg mice using primers in the 3′ end of the human α-skeletal actin promoter (5′-AAGCCAAAGTCCTAATGTGC A-3′) and a sequence within TRPV2 (5′-AATGAATTCGT AGTTGAGATTCACTTTAAT-3′). Normal and abnormal dystrophin genes were detected by PCR using the following primers: sense primer, 5′-AACTCATCAAATATGCGTGTTA GTG-3′; antisense primer for normal dystrophin, GTCACTCA-GATAGTTGAAGCCATTTTAA; antisense primer for abnormal dystrophin present in *mdx* mice, GTCACTCAGATATA GTTGAAGCCATTTAG.

Animal experiments

All animal experiments were performed according to the Guidelines for Animal Experimentation at the National Cardiovascular Center. Muscle strength was evaluated by a grip-test as previously described (28). Briefly, mice were placed to hold onto a fine wire net with their forelimbs and the length of the time they could support their body weight was recorded. CK activity was measured as previously described (28).

Histology

Skeletal muscle was fixed in phosphate buffer saline (PBS) containing 10% formalin and embedded in paraffin. Serial sections (5 μm) were stained with hematoxylin and eosin (H&E) or Masson's trichrome for morphological analysis. The extent of muscle regeneration was determined by counting the number of fibers with central nuclei. The variability in fiber size was determined by averaging the standard deviations of the area from the myofiber cross-sectional views (>1000 fibers) of three to four animals per group (28). To detect apoptosis, muscle fibers were TUNEL stained using an apoptosis detection kit (Takara Biomedical). For the measurement of EBD uptake, EBD in PBS (10 mg/ml) was injected intraperitoneally into each kind of mice (0.1 ml/10 g body weight). The mice were sacrificed 24 h after injection. Muscles were excised and embedded in optimal cutting temperature compound (Tissue-Tek, Torrence, CA, USA) and snap-frozen using liquid nitrogen. Blocks were then sectioned into 6-μm thick slices, dried for 10 min and washed briefly in PBS. The EBD was detected as red auto-fluorescence. All histochemical analysis was done by investigators blinded to genotype.

Quantification of histological data

Stained serial sections were viewed under a light microscope (OLYMPUS BX41) and images were analyzed using a computer-assisted imaging system (FLOVEL Filing System) by investigators blinded to the genotypes. Images were acquired using a digital camera (Olympus FX380) equipped with image filing software (Flovel FLVFS-LS, Tokyo, Japan). The extent of damage occurring in muscles was determined by comparing the

number of centrally located nuclei (CLN) between samples. The variability of fiber size was obtained by averaging the standard deviations of cross-sectional myofiber views. Fibrosis was assessed by measuring the Masson's trichrome-positive area. Briefly, color images were converted to binary images by setting a threshold so only blue-stained fibrotic areas were detected. These areas were summed and reported as a percentage of the total area. The infiltrate area was defined as the region infiltrating non-muscle cells, such as lymphocytes and macrophages, and showing the accumulation of small nuclei and weak staining with eosin. Such areas were selected by eye and represented as the percentage of the total area.

Immunoblot and immunohistochemistry

Immunoblotting and immunohistochemistry were carried out as previously described (16,34). Briefly, the immunoblot was visualized using an enhanced chemiluminescence detection system (Amersham Biosciences) after blotting, blocking with PBS containing 5% non-fat milk and incubation with the appropriate primary and horseradish peroxidase-conjugated secondary antibodies. For immunohistochemistry, several different procedures were used. Frozen muscle sections (5–6 μm thick) or methanol fixed myotubes were double immunostained by incubating for 1 h with fluorescein isothiocyanate (FITC)-conjugated rat anti-HA antibody and rabbit anti-TRPV2 antibody, followed by further incubation with rhodamine-conjugated secondary antibody. Frozen muscle sections were also immunostained with anti-dystrophin antibody. For the immunostaining of isolated fibers, fibers immobilized on glass slides were fixed with 4% paraformaldehyde for 15 min at room temperature, permeabilized with 0.1% TritonX-100 and then stained with anti-TRPV2 antibody followed by FITC-conjugated secondary antibody. Stained samples were observed by a confocal laser scanning microscopy (FLUOVIEW FV1000, Olympus) mounted on an objective lens (Olympus). Serial sections of BIO14.6 skeletal muscles were immunostained with an enzymatic color detection system. Sections were incubated with anti-HA or anti-TRPV2 overnight, then treated with Simple Stain MAX-PO (NICHIREI CO.) for rat antibody or DAKO EnVision^{TM}+System (Peroxidase) for rabbit antibody, followed by color development with diaminobenziden (DAB). Samples were observed by a light microscope (OLYMPUS BX41).

Isolation of fibers

FDB muscles were removed and incubated for 40 min at 37°C in Krebs solution containing 124 mM NaCl, 1.2 mM $MgCl_2$, 5.9 mM KCl, 11.5 mM glucose, 11.5 mM Hepes-Na, 1.5 mM $CaCl_2$ and 0.2% collagenase type IV (Sigma-Aldrich). Muscles were then removed, washed twice in Krebs buffer and suspended in Ham's F12/DME (Sigma-Aldrich) supplemented with 2% FCS. Single fibers were mechanically dissociated by repeatedly passing the muscle through fire-polished Pasteur pipettes. Dissociated fibers were plated onto glass-bottom dishes coated with BDcell-Tak^{TM} (BD Biosciences) and allowed to adhere to the bottom of the dish for 2 h.

Cell culture, plasmid transfection and myotube preparation

Chinese hamster ovary (CHO-K1) cells and corresponding transfectants were maintained in DMEM containing 25 mM $NaHCO_3$ and supplemented with 7.5% (v/v) fetal calf serum. cDNAs were transfected into CHO cells with Lipofectamine 2000 (Invitrogen Corp., CA, USA) and stable clones were isolated after selection with puromycin or G418. Myotube culture was performed using muscles from normal or BIO14.6 hamsters by enzymatic dissociation essentially as described previously (35). Briefly, we prepared satellite cells from the gastrocnemius muscle of hamsters using an enzyme cocktail containing 0.5 mM $CaCl_2$ for cell dissociation. After enrichment of the myoblasts by several preplatings, cells were placed on the culture dishes; 2 days later, culture medium was switched to DMEM containing 2% horse serum to induce myotube formation. Two to 4 days after start of fusion, the generated myotubes were analyzed.

Application of stretch

Myotubes were subjected to a uniaxial sinusoidal stretch of up to 120% at 1 Hz and 25°C for 1 h using a temperature-controlled stretching apparatus (NS-300; SCHOLAR-TEC Co., Osaka, Japan) as described previously (36). Cells were cultured in a silicon-rubber chamber with 400 μm thick side walls and a 200 μm thick transparent bottom coated with collagen I. In this way, uniform stretch was applied to most of cells cultured on the bottom (36). Osmotic stress-induced cell damage was observed in myofibers preloaded with 5 μM calcein-AM as previously described (15).

Ca^{2+} measurement

CHO cells and HEK293 cells were loaded with 4 μM fura-2 acetoxymethyl ester (fura-2/AM) for 30 min at 37°C, and maintained in balanced salt solution (BSS) (146 mM NaCl, 4 mM KCl, 2 mM $MgCl_2$, 0.5 mM $CaCl_2$, 10 mM glucose, 0.1% bovine serum albumin and 10 mM HEPES/Tris, pH7.4); fura-2 fluorescence was measured by a ratiometric fluorescence method using a fluorescence image processor (Aquacosmos, Hamamatsu Photonics). The excitation wavelength was alternated at 340 and 380 nm (1 Hz), and the emitted fluorescence light was detected at 510 nm. The fluorescence ratio at 340/380 nm was calculated and $[Ca^{2+}]_i$ was determined using a K_d of 135 nM for the dissociation of fura-2/Ca^{2+} complex (37). Muscle fibers were loaded for 1 h at room temperature with 4 μM fura-2/AM in BSS. For the experiments, the working medium contained 50 μM N-benzyl-p-toluene sulphonamide (BTS), an inhibitor of the myosin II ATPase. Stimulation with 2APB was performed in BSS containing 5 mM $CaCl_2$ (pH6.8). Myotubes were loaded with 4 μM fluo-4 acetoxymethyl ester for 30 min at 37°C, and maintained in BSS. Fluorescence signal was detected with a confocal microscope (MRC-1024; Bio-Rad, Richmond, CA, USA) mounted on an Olympus BX50WI microscope. Images were acquired at a rate of one image every 1 s and single-frames or the single cell-integrated signal density were analyzed by Laser-Sharp software (Bio-Rad). All Ca^{2+} measurements were carried out at room temperature.